Orientation selection in dendritic evolution

TOMORR HAXHIMALI[1], ALAIN KARMA[1]*, FRÉDÉRIC GONZALES[2] AND MICHEL RAPPAZ[2]

[1]Department of Physics and Center for Interdisciplinary Research on Complex Systems, Northeastern University, Boston, Massachusetts 02115, USA
[2]Computational Materials Laboratory, Institute of Materials, School of Engineering, Ecole Polytechnique Fédérale de Lausanne, Station 12, CH-1015 Lausanne, Switzerland
*e-mail: A.karma@neu.edu

Published online: 9 July 2006; doi:10.1038/nmat1693

Dendritic crystal growth patterns have fascinated scientists for several centuries. Much of the aesthetic appeal of these patterns stems from the hierarchical structure of primary-, secondary-, and higher-order branches, which typically grow along principal crystallographic axes. Atypical growth directions have also been observed. Here, we demonstrate both computationally and experimentally that the range of possible dendrite growth directions, and hence the morphological diversity of the resulting dendritic structures, is much richer than previously anticipated. In particular, we show that primary dendrite growth directions can vary continuously between different crystallographic directions as a function of the composition-dependent anisotropy parameters. The study combines phase-field simulations of equiaxed dendritic growth and directional freezing of Al–Zn alloys. Both simulations and experiments exhibit continuous changes of direction from ⟨100⟩ to ⟨110⟩ for an underlying cubic symmetry. These results have important implications for controlling the microstructure of a wide range of cast alloys that solidify dendritically.

Dendritic alloy microstructures are formed during a wide range of solidification processes from casting to welding. These microstructures result from a morphological instability of the solid–liquid interface that produces dendrites, which are highly hierarchical branched patterns with primary-, secondary- and higher-order branches. As alloy impurities segregate in the interdendritic liquid during solidification, the spatially inhomogeneous distribution of impurities in the completely solidified alloy is a direct footprint of the dendritic network that formed and coarsened during the solidification process. It also determines the formation and distribution of secondary phases, and thus has a profound influence on the properties of a wide range of technologically important structural materials, from light-weight aluminium alloys used in the automotive industry to nickel-based superalloys used for turbine blades. The study of dendritic growth[1,2] has also been of long-standing fundamental interest because of the ubiquity of branched structures exhibited by diverse interfacial pattern formation systems[3–5].

Major theoretical and computational advances over the past two decades have improved our fundamental understanding of dendrite growth, as well as new capabilities to simulate and predict dendritic microstructures on experimentally relevant length and timescales[6] and to elucidate new pattern formation mechanisms[7,8] that enlarge the scope of our understanding of these structures. The commonly accepted microscopic solvability theory of steady-state dendrite growth[9–12], which builds on the earlier diffusive transport theory of Ivantsov[13], has led to the understanding that crystalline anisotropy is a crucial parameter that uniquely determines the growth rate and tip radius of dendrites, which is the basic scaling length for the entire dendritic network. Predictions of this theory have been largely validated by phase-field simulations of dendritic evolution over the past few years for both small[14–19] and large[20] growth rate. Moreover, molecular dynamics (MD) simulation methods[21–30] as well as experimental techniques[31,32] have recently been developed to accurately compute anisotropic interfacial properties that control dendritic evolution.

Despite this progress, dendrite growth theory remains limited to predicting the steady-state characteristics of dendrites growing along simple crystallographic directions, such as the ⟨100⟩ directions that correspond to the main crystal axes for materials with cubic symmetry, or the six directions in the basal plane of

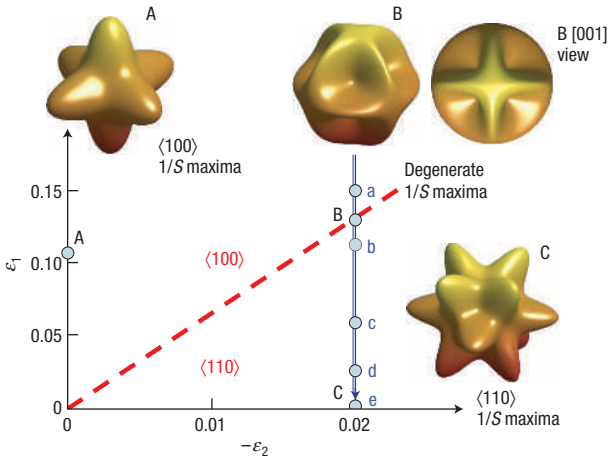

Figure 1 Orientation selection map from minimum interfacial stiffness. The axes ε_1 and ε_2 are the coefficients of the first two cubic harmonics that characterize the anisotropy of the interfacial free energy γ. The interfacial stiffness S has minima that correspond to ⟨100⟩ and ⟨110⟩ above and below the red dashed line ($\varepsilon_1 = -20\varepsilon_2/3$), respectively. There is a continuous degeneracy of orientation on this line where all directions contained in {100} planes have equal stiffness minima. Illustrative spherical plots of $1/S$ are also shown for: A, ⟨100⟩ ($\varepsilon_2 = 0$, $\varepsilon_1 = 0.11$), B, degenerate minima ($\varepsilon_2 = -0.02$, $\varepsilon_1 = 0.13$), and C, ⟨110⟩ ($\varepsilon_2 = -0.02$, $\varepsilon_1 = 0$). The lower-case letters (a–e) correspond to the parameters of the phase-field simulations shown in Fig. 2.

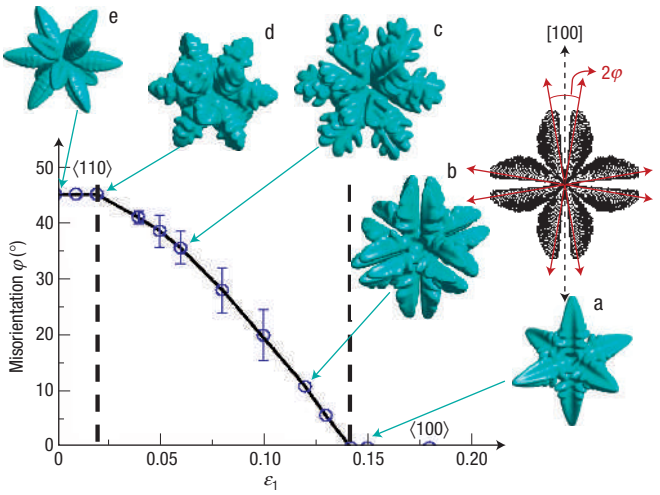

Figure 2 Equiaxed dendrites and growth directions from phase-field simulations. Phase-field simulations showing the different equiaxed growth morphologies obtained for different values of ε_1 at fixed $\varepsilon_2 = -0.02$, following the blue arrow (a–e) that crosses the degenerate ⟨100⟩–⟨110⟩ boundary. Instead of making an abrupt change from ⟨100⟩ to ⟨110⟩ as this boundary is crossed, the misorientation φ increases continuously from $\varphi = 0$ (⟨100⟩ dendrites) to 45° (⟨110⟩ dendrites) over a large range of ε_1 between the two dashed lines. The error bars reflect the uncertainty associated with the change of growth orientation during the slow relaxation to steady-state growth. The image in the upper right-hand side shows two-dimensional cross-sections of the solid–liquid boundary at equal intervals of time in a (001) plane for parameters corresponding to point b. It illustrates the divergent growth of misoriented dendrites.

hexagonal symmetry crystals. This theory falls short of predicting a host of other directions that have been observed experimentally, ranging from early observations of ⟨22$\underline{4}$5⟩ directions off the basal plane and the c axis in Mg alloys with hexagonal crystal symmetry[33,34] as well as ⟨110⟩ and ⟨111⟩ directions for ammonium chloride in aqueous solutions[35], to more recent observations of ⟨110⟩, ⟨320⟩, ⟨211⟩, and even unsteady curvilinear dendrite paths in face-centred cubic (f.c.c.) Al-based alloys[36–41].

These observations raise the question of what the fundamental relationship between dendrite growth directions and the underlying crystal symmetry is. In this paper, the question of orientation selection is explored using both phase-field simulations of three-dimensional equiaxed growth for cubic anisotropy and electron back-scattered diffraction (EBSD) analysis of dendrite growth directions in f.c.c. Al–Zn alloys as a function of Zn composition. The simulations exploit new knowledge of the anisotropy of the interfacial energy recently obtained from MD simulations[21]. Our main finding is that dendrite growth directions are not limited to a discrete set of crystallographic directions, as would be expected from the anisotropy of the interfacial free-energy. Instead, the growth directions can vary continuously over some range of anisotropy parameters. Moreover, values of these parameters computed from molecular dynamics simulations for pure f.c.c. metals (such as Al, Ni, Cu, etc) fall close to this range, which has important consequences for the control of dendritic microstructures in alloys of technological relevance.

When the attachment kinetics of atoms at the interface is rapid, which is the case for most metal systems[21], the solid–liquid interface can be assumed to be locally in thermodynamic equilibrium for small to moderate dendrite growth rates that prevail in most processing conditions. Dendrite growth directions must then be determined primarily by the anisotropy of the solid–liquid interfacial energy, $\gamma(\hat{n})$, where $\hat{n}$ is the direction normal to the interface. For crystals with an underlying cubic symmetry, $\gamma(\hat{n})$ can be expanded in the form:

$$\gamma(\theta,\varphi) = \gamma_0[1 + \varepsilon_1 K_1(\theta,\varphi) + \varepsilon_2 K_2(\theta,\varphi) + \cdots], \qquad (1)$$

where γ_0 is the mean value of γ, θ and φ are the spherical angular coordinates of the interface normal, ε_1 and ε_2 are the anisotropy parameters and K_1 and K_2 are cubic harmonics that are combinations of standard spherical harmonics $Y_{lm}(\theta,\varphi)$ with cubic symmetry[21,35,42,43]. Historically, dendrite growth has been modelled primarily using the first cubic harmonic for positive ε_1, which favours the commonly observed ⟨100⟩ dendrite growth directions. However, recent MD simulation[21] studies have revealed that it is also necessary to retain the second term in this expansion to accurately describe the entire γ-plot, that is, $\gamma(\hat{n})$, for all orientations. Moreover, they have shown that, for a wide range of f.c.c. metals, ε_2 is negative whereas ε_1 is positive. As a positively weighted first cubic harmonics favours ⟨100⟩ directions, whereas a negatively weighted second cubic harmonics favours ⟨110⟩ directions[35], it is not *a priori* obvious whether ⟨100⟩, ⟨110⟩ or some other direction will be favoured under the combined effect of both cubic harmonics.

A first approximate answer to this question, which sets the stage for the phase-field simulations, can be obtained by assuming that dendrites will pick easy growth directions where capillary forces are weakest, and hence least effective at smoothing out protrusions of the solid–liquid interface. Capillary forces enter the dendrite growth problem through the classic Gibbs–Thomson condition, which relates the local equilibrium temperature or composition of a curved interface to the interface stiffness and curvature. In two dimensions, the stiffness is a scalar quantity $\gamma + \mathrm{d}^2\gamma/\mathrm{d}\theta^2$, where θ is

the angle between $\hat{n}$ and a fixed reference axis. For the simple form $\gamma = \gamma_0(1+\varepsilon_4\cos 4\theta + \cdots)$, commonly assumed in theoretical studies of dendrite growth, and positive ε_4, stiffness minima correspond to $\langle 10 \rangle$ dendrite growth directions. In three dimensions, the interface stiffness becomes a tensor, $\gamma\delta_{ij} + \partial^2\gamma/\partial\varphi_i\partial\varphi_j$, where φ_1 and φ_2 measure the local deviation of $\hat{n}$ along two orthogonal directions in a plane perpendicular to $\hat{n}$, and δ_{ij} is the standard Kronecker delta defined such that $\delta_{ij} = 1$ for $i = j$ and $\delta_{ij} = 0$ for i different from j. Easy growth directions can then be identified by minima of the trace of this stiffness tensor referred to hereafter simply as the stiffness

$$S = 2\gamma + \frac{\partial^2\gamma}{\partial\theta^2} + \frac{1}{\sin^2\theta}\frac{\partial^2\gamma}{\partial\varphi^2} + \cot\theta\frac{\partial\gamma}{\partial\theta}, \qquad (2)$$

which is expressed above in terms of the spherical angular coordinates.

We have used equations (1) and (2) together with the known analytical forms of the cubic harmonics[21,42,43] to make spherical plots of the inverse of the stiffness $1/S$ as a function of orientation $\hat{n}$ for different anisotropy parameters. Stiffness minima, which correspond to maxima of $1/S$, are clearly seen as bumps on these plots. Results are shown in Fig. 1 together with an orientation selection map in the anisotropy parameter space relevant for f.c.c. metals, that is, the $(\varepsilon_2, \varepsilon_1)$ plane for positive ε_1 and negative ε_2. This map shows the existence of two distinct regions with stiffness minima corresponding to $\langle 100 \rangle$ and $\langle 110 \rangle$ respectively, separated by a boundary, which can be shown analytically to be a straight line $\varepsilon_1 = -20\varepsilon_2/3$. Away from this boundary towards the positive ε_1 axis, there are well-developed $\langle 100 \rangle$ stiffness minima ($1/S$ maxima), which are expected to favour $\langle 100 \rangle$ dendrite growth directions. Similarly, away from this boundary towards the negative ε_2 axis, well-developed $\langle 110 \rangle$ stiffness minima should favour $\langle 110 \rangle$ growth directions. However, exactly on the $\langle 100 \rangle$–$\langle 110 \rangle$ boundary, all directions comprised in any of the {100} planes correspond to stiffness minima. This degeneracy is best illustrated by viewing the $1/S$ plot from the [001] direction for an $(\varepsilon_2, \varepsilon_1)$ pair on this boundary, as shown in Fig. 1. The outer perimeter of this plot, which spans the orientations $\hat{n} = \cos\varphi\,\hat{x} + \sin\varphi\,\hat{y}$ for $\varphi \in [0, 2\pi]$ is perfectly circular, such that all φ have equal stiffness minima. This degeneracy suggests that dendrite growth directions are not strongly determined by stiffness minima near the $\langle 100 \rangle$–$\langle 110 \rangle$ boundary in the $(\varepsilon_2, \varepsilon_1)$ plane. Therefore, although the minimum stiffness criterion predicts a discontinuous change from $\langle 100 \rangle$ to $\langle 110 \rangle$ directions as this boundary is crossed, it is unclear whether this criterion will hold true when stiffness minima are not pronounced.

To test these predictions, we carried out three-dimensional phase-field simulations of equiaxed dendritic growth in a pure undercooled melt. We used a well-established methodology[14–18] to carry out quantitative simulations at low undercooling, which was previously used to study $\langle 100 \rangle$ dendrites with a single anisotropy parameter $\varepsilon_1 > 0$ and $\varepsilon_2 = 0$. The present simulations only differ by the incorporation of two anisotropy parameters with γ defined by equation (1). Although we focus on the solidification of a pure melt, we also expect the results to apply to the equiaxed isothermal solidification of binary alloys given the well-known mathematical isomorphism between the two problems. The simulations were carried out for a fixed undercooling that is 10% of the ratio of the latent heat of melting to the specific heat. The simulations used a small spherical crystal seed as the initial condition and tracked its evolution into a well-developed equiaxed structure with well-defined dendrite growth directions that were constant at large time.

Figure 2 shows the equiaxed dendrites obtained when crossing the $\langle 100 \rangle$–$\langle 110 \rangle$ boundary vertically, that is, by fixing ε_2 and lowering ε_1 from a sufficiently large value where $\langle 100 \rangle$ dendrites are selected to $\varepsilon_1 = 0$. Each pair of $(\varepsilon_2, \varepsilon_1)$ values corresponds to a different simulation starting from a spherical seed. The results reveal that the transition between $\langle 100 \rangle$ and $\langle 110 \rangle$ is not discontinuous, as predicted by the minimum stiffness criterion. In contrast, the growth direction changes continuously from $\langle 100 \rangle$ to $\langle 110 \rangle$ as a function of ε_1. The directions are contained in the {100} planes and the misorientation, that is, the angle φ between growth directions in these planes and the principal crystal axes, varies from 0 to $\pi/4$. By symmetry, structures for $0 < \varphi < \pi/4$ are 'hyperbranched', exhibiting 24 branches growing simultaneously, as opposed to 6 and 12 branches for $\langle 100 \rangle$ ($\varphi = 0$) and $\langle 110 \rangle$ ($\varphi = \pi/4$) dendrites, respectively. The robustness of the results was checked by carrying out a few lengthy simulations without enforcing the crystal symmetry. These simulations yielded identical results as those that enforce the crystal symmetry to make computations more efficient. The continuous change of orientation was also found to be independent of undercooling in a low-undercooling regime.

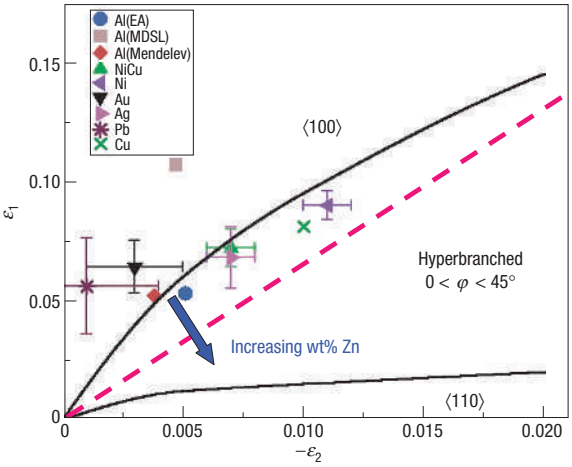

Figure 3 Orientation selection map from phase-field simulations. Map of the different regions corresponding to $\langle 100 \rangle$ and $\langle 110 \rangle$ dendrites above and below the two solid lines, respectively, and hyperbranched dendrites with a continuous change of misorientation from 0 to 45° in between these two lines. The anisotropy parameters for different f.c.c. metals and one f.c.c. metallic alloy obtained from molecular dynamics simulations with the corresponding error bars[21] are superimposed. The blue arrow is a putative guess of the change of anisotropy parameters induced by Zn addition to Al.

Figure 3 shows the results of an exhaustive numerical survey of the anisotropy parameter space that distinguishes the three domains of $\langle 100 \rangle$, hyperbranched, and $\langle 110 \rangle$ dendrites in the $(\varepsilon_2, \varepsilon_1)$ plane, together with anisotropy parameters for f.c.c. and body-centred cubic metals determined from MD simulations. Two main features stand out. First, hyperbranched dendrites whose primary branches are misoriented with respect to crystal axes occupy a large fraction of this plane, whereas the $\langle 110 \rangle$ dendrites are constrained to a narrow wedge above the negative ε_2 axis. Second, the MD data for several pure f.c.c. metals (Table III from ref. 21) fall strikingly close to the $\langle 100 \rangle$-hyperbranched boundary. Therefore, it is natural to hypothesize that the change of anisotropy parameters resulting from solute addition is the underlying mechanism for atypical dendrite growth directions observed in some f.c.c. metallic alloys[36–41]. This seems likely because only small changes are necessary to shift the anisotropy parameters either above or below this boundary.

To test this hypothesis experimentally, we have analysed dendrite growth directions in solidified Al–Zn alloys. This alloy was chosen because a previous study[40,41] of Al–45 wt% Zn coatings deposited on steel sheets revealed atypical ⟨320⟩ dendrite growth directions in grains with various orientations with respect to the coating surface. Therefore, a systematic study of growth directions as a function of increasing Zn composition would be expected to reveal the change of growth direction from ⟨100⟩ for dilute Zn composition to atypical directions for larger Zn composition. Several Al–Zn alloys were prepared, from 99.995% purity Al and 99.995% purity Zn, with 5, 10, 25, 30, 35, 45, 50, 55, 65, 75 and 90 wt% Zn. These alloys were solidified in a Brigdman furnace at 67 $\mu m\,s^{-1}$ and in a directional solidification (DS) setup at a velocity varying between 0.5 and 3 $mm\,s^{-1}$, depending on the height of the specimen. The dendritic microstructure of chemically etched and electropolished longitudinal sections of solidified alloys was analysed using a combination of standard optical or scanning electron microscopy and EBSD orientation measurements. For each specimen, several grains in which dendrite primary trunks were perfectly aligned with the metallographic section were identified. The steady-state dendrites in these grains showed well-defined primary trunks and side arms, the orientation of which was measured by EBSD (error estimation of 2° for the angle φ between the trunks and the ⟨100⟩ reference direction).

The experimental results are summarized in Fig. 4. The key finding is that the change of dendrite growth direction as a function of Zn composition directly mirrors the change of growth direction as a function of anisotropy in the phase-field simulations (Fig. 2). In particular, ⟨100⟩ directions only exist up to a critical Zn composition (25 wt%). For a concentration higher than 55 wt%, the dendrites are clearly growing along ⟨110⟩ directions as indicated in Fig. 4 for an Al–90 wt% Zn (right inset). As shown by the circle and square symbols, associated with Bridgman and DS specimens respectively, the results do not depend on the type of experiments, thus showing their independence with respect to the velocity. This eliminates the contribution of attachment kinetics anisotropy in the present experiments, thus supporting a continuous change of steady-state dendrite orientation dictated only by the surface energy anisotropy variation, as in the phase-field simulations. This is in contrast to other DS experiments where abrupt velocity-dependent transitions between slow ⟨100⟩ and fast ⟨111⟩ growth modes have been related to the anisotropic departure from local chemical equilibrium at the solid–liquid interface for ammonium chloride dendrites[44]. For concentrations between 25 and 55 wt% Zn, the misorientation of the dendrite trunks continuously increases from 0 to 45°. The left inset in Fig. 4 shows the steady-state dendrite trunks for an Al–50 wt% Zn which are close to a ⟨320⟩ direction. One interesting difference between the phase-field simulations of equiaxed growth and the directional growth experiments is the observation, in the latter, of more-disordered seaweed structures at the beginning and at the end of the dendrite orientation transition (that is, around 25 and 55 wt% Zn). However, these seaweeds exhibit a well-defined orientation texture in DS specimens where many grains form at the bottom, thus indicating that a selection mechanism based on a preferred orientation has nevertheless occurred during grain growth competition. This preferred orientation indicated by the mean texture direction of the seaweed structure (filled symbols in Fig. 4) follows the general trend predicted for the dendrite orientation transition.

The striking similarity between the computational and the experimental results strongly support the hypothesis that the change of anisotropy parameters with Zn composition is the underlying mechanism of the change of growth direction observed experimentally, as indicated by the blue arrow in Fig. 3. This

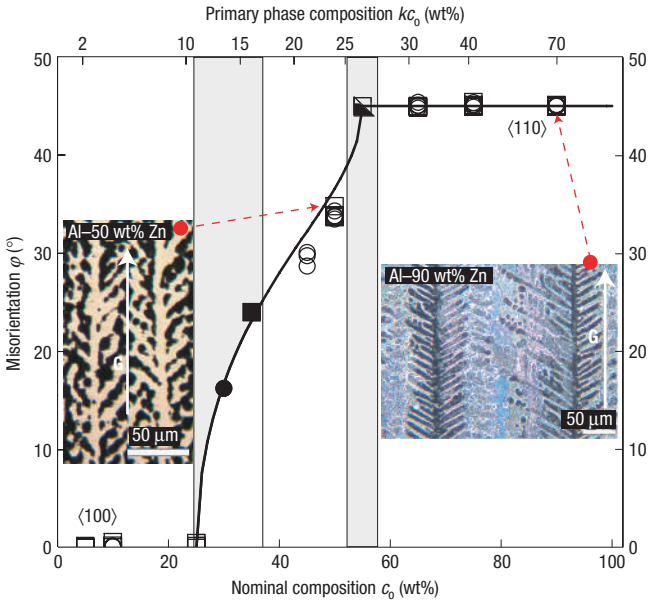

Figure 4 Columnar dendrites and growth directions from experiments. Plot of the dendrite growth misorientation obtained from microstructural analysis of directionally solidified Al–Zn alloys as a function of Zn composition showing a continuous increase from 0 to 45° over a finite range of Zn composition, comprised between ⟨100⟩ and ⟨110⟩ dendrites for dilute and concentrated alloys. The Bridgman experiments were done at 67 $\mu m\,s^{-1}$ in a gradient of 100 $K\,cm^{-1}$, whereas in the directional solidification experiments, the velocity varied between 3 and 0.5 $mm\,s^{-1}$ and the gradient from 30 $K\,cm^{-1}$ to 0 depending on the distance from the bottom water-cooled surface. Open squares and circles correspond to directionally solidified and Bridgman specimens, respectively. Filled symbols have been used for textured seaweeds. Insets: micrographs of dendrites in longitudinal sections of Bridgman specimens corresponding to Al–50 wt% Zn (left, ⟨320⟩ growth) and Al–90 wt% Zn (right, ⟨110⟩ growth).

interpretation is supported by the fact that the dendrite tip composition is close to the nominal composition of the alloy for the range of growth rates in the experiments, thereby making the correlation of growth direction and composition valid. A further test of this hypothesis would require a determination of crystalline anisotropy parameters in Al–Zn alloys using either MD simulations or equilibrium shape measurements.

These results bring new challenges for dendritic growth theory. The commonly accepted theory uses the Ivantsov transport theory[13] to relate the product ρV of the dendrite tip radius ρ and velocity V to the tip undercooling (or tip supersaturation for alloys), together with a solvability condition for the existence of steady-state needle crystal solutions[9–12]. The latter relates the product $\rho^2 V$ to the capillary anisotropy, thereby uniquely determining ρ and V independently. We have used this theory to predict the growth rate and limit of existence of ⟨100⟩ dendrites in the $(\varepsilon_2, \varepsilon_1)$ plane. The predictions were found to be in good quantitative agreement with the phase-field simulations. However, this theory falls short of independently predicting the steady-state operating state of the dendrite tip and its growth direction ($\rho^2 V$ and the misorientation φ) in three dimensions. This prediction is currently only possible in two dimensions[45]. In addition, the minimum stiffness criterion only predicts ⟨100⟩ or ⟨110⟩ directions (Fig. 2) within a description of γ with only two cubic harmonics. This criterion is mainly useful to identify a region of the anisotropy parameter space where a continuous variation of misorientation may occur, close to a boundary between two discrete sets of

directions where stiffness minima are degenerate (Fig. 2), but cannot fundamentally predict this variation. Hence, a general theory capable of predicting dendrite growth directions in three dimensions is still lacking.

In summary, we have demonstrated both computationally and experimentally that orientation selection in dendritic evolution is considerably richer than previously expected. Dendrite growth directions encompass a continuous range of misorientations, which dramatically enlarges the scope of possible dendritic patterns that can be expected to form in nature. The fact that misoriented dendritic microstructures cover a large region of the anisotropy parameter space relevant for metallic alloys suggests that these microstructures may be more common than previously thought, consistent with their existence over a wide range of composition in the present experiments. Moreover, the possibility of altering anisotropy parameters, and hence orientation selection, by the addition of solute elements (such as Zn or Mg for Al alloys) offers new prospects to control dendritic microstructures and optimize material behaviour in a wide range of applications.

Received 9 March 2006; accepted 6 June 2006; published 9 July 2006.

References

1. Langer, J. S. Instabilities and pattern formation in crystal growth. *Rev. Mod. Phys.* **52,** 1–28 (1980).
2. Karma, A. in *Branching in Nature* (eds Fleury, V., Gouyet, J. F. & Lonetti, M.) Ch. XI, 365 (Les Houches, vol. 13, EDP Sciences, Springer, 2001).
3. Trivedi, R., Liu, S. & Williams, S. Interface pattern formation in nonlinear dissipative systems. *Nature Mater.* **1,** 157–159 (2002).
4. Ben-Jacob, E. & Garik, P. The formation of patterns in non-equilibrium growth. *Nature* **343,** 523–530 (1990).
5. Fleury, V. Branched fractal patterns in non-equilibrium electrochemical deposition from oscillatory nucleation and growth. *Nature* **390,** 145–148 (1997).
6. Boettinger, W. J., Warren, J. A., Beckermann, C. & Karma, A. Phase-field simulation of solidification. *Ann. Rev. Mater. Res.* **32,** 163–194 (2002).
7. Gránásy, L. *et al.* Growth of 'dizzy dendrites' in a random field of foreign particles. *Nature Mater.* **2,** 92–96 (2003).
8. Gránásy, L., Pusztai, T., Börzsönyi, T., Warren, J. A. & Douglas, J. F. A general mechanism of polycrystalline growth. *Nature Mater.* **2,** 645–650 (2003).
9. Langer, J. S. in *Chance and Matter* (eds Souletie, J., Vannimenus, J. & Stora, R.) 629–711 (Les Houches, Session XLVI, North Holland, Amsterdam, 1987).
10. Barbieri, A. & Langer, J. S. Predictions of dendritic growth rates in the linearized solvability theory. *Phys. Rev. A* **39,** 5314–5325 (1989).
11. Kessler, D., Koplik, J. & Levine, H. Pattern selection in fingered growth phenomena. *Adv. Phys.* **37,** 255–339 (1988).
12. Ben Amar, M. & Brener, E. Theory of pattern selection in three dimensional nonaxisymmetric dendritic growth. *Phys. Rev. Lett.* **71,** 589–592 (1993).
13. Ivantsov, G. P. Temperature field around spheroidal, cylindrical and acicular crystal growing in a supercooled melt. *Doklady Akad. Nauk. SSSR* **58,** 567–569 (1947).
14. Karma, A. & Rappel, W. J. Numerical simulations of three-dimensional dendritic growth. *Phys. Rev. Lett.* **77,** 4050–4053 (1996).
15. Karma, A. & Rappel, W. J. Quantitative phase-field modeling of dendritic growth in two and three dimensions. *Phys. Rev. E* **57,** 4323–4349 (1998).
16. Karma, A. Phase-field methods. *Encyclopedia of Materials: Science and Technology* **7,** 6873–6886 (2001).
17. Plapp, M. & Karma, A. Multiscale random-walk algorithm for simulating interfacial pattern formation. *Phys. Rev. Lett.* **84,** 1740–1743 (2000).
18. Plapp, M. & Karma, A. Multiscale finite-difference-diffusion-Monte-Carlo method of simulating dendritic solidification. *J. Comp. Phys.* **165,** 592–619 (2000).
19. Provatas, N., Goldenfeld, N. & Dantzig, J. Efficient computation of dendritic microstructures using adaptive mesh refinement. *Phys. Rev. Lett.* **80,** 3308–3311 (1998).
20. Bragard, J., Karma, A., Lee, Y. H. & Plapp, M. Linking phase-field and atomistic simulations to model dendritic solidification in highly undercooled melts. *Interface Sci.* **10,** 121–136 (2002).
21. Hoyt, J. J., Asta, M. & Karma, A. Atomistic and continuum modeling of dendritic solidification. *Mater. Sci. Eng. R* **41,** 121–163 (2003).
22. Hoyt, J. J., Asta, M. & Karma, A. Method for computing the anisotropy of the solid-liquid interfacial free energy. *Phys. Rev. Lett.* **86,** 5530–5533 (2001).
23. Hoyt, J. J. & Asta, M. Atomistic computation of liquid diffusivity, solid-liquid interfacial free energy, and kinetic coefficient in Au and Ag. *Phys. Rev. B* **65,** 214106 (2002).
24. Hoyt, J. J., Asta, M. & Karma, A. Atomistic simulation method for computing the kinetic coefficient in solid-liquid systems. *Interface Sci.* **10,** 181–189 (2002).
25. Asta, M., Hoyt, J. J. & Karma, A. Calculation of alloy solid-liquid interfacial free energies from atomic-scale simulations. *Phys. Rev. B* **66,** 100101 (2002).
26. Sun, D. Y., Asta, M., Hoyt, J. J., Mendelev, M. I. & Srolovitz, D. J. Crystal-melt interfacial free energies in metals:fcc versus bcc. *Phys. Rev. B* **69,** 020102 (2004).
27. Sun, D. Y., Asta, M. & Hoyt, J. J. Crystal-melt interfacial free energies and mobilities in fcc and bcc Fe. *Phys. Rev. B* **69,** 174103 (2004).
28. Sun, D. Y., Asta, M. & Hoyt, J. J. Kinetic coefficient of Ni solid-liquid interfaces from molecular-dynamics simulations. *Phys. Rev. B* **69,** 024108 (2004).
29. Morris, J. R. The complete mapping of the anisotropic free energy of the crystal-melt interface in Al. *Phys. Rev. B* **66,** 144104 (2002).
30. Sun, D. Y. *et al.* Crystal-melt interfacial free energies in hcp metals: A molecular dynamics study of Mg. *Phys. Rev. B* **73,** 024116 (2006).
31. Liu, S., Napolitano, R. E. & Trivedi, R. Measurement of anisotropy of crystal-melt interfacial energy for a binary Al-CU alloy. *Acta Mater.* **49,** 4271–4276 (2001).
32. Napolitano, R. E. & Liu, S. Three-dimensional crystal-melt Wulff-shape and interfacial stiffness in the Al-Sn binary system. *Phys. Rev. B* **70,** 214103 (2004).
33. Pettersen, K. & Ryum, M. Crystallography of directionally solidified Magnesium alloy AZ91. *Metall. Trans. A* **20,** 847–852 (1989).
34. Pettersen, K., Lohne, O. & Ryum, M. Dendritic solidification of Magnesium alloy AZ91. *Metall. Trans. A* **21,** 221–230 (1990).
35. Chan, S.-K., Reimer, H.-H. & Kahlweit, M. On the stationary growth shapes of NH_4Cl dendrites. *J. Cryst. Growth* **32,** 303–315 (1976).
36. Henry, S., Jarry, P., Jouneau, P.-H. & Rappaz, M. Electron backscattered diffraction investigation of the texture of feathery crystals in aluminum alloys. *Metall. Mater. Trans. A* **28A,** 207–213 (1997).
37. Henry, S., Jarry, P. & Rappaz, M. ⟨110⟩ Dendrite growth in aluminum feathery grains. *Metall. Mater. Trans. A* **29A,** 2807–2817 (1998).
38. Henry, S., Minghetti, T. & Rappaz, M. Dendrite growth morphologies in aluminium alloys. *Acta Mater.* **46,** 6431–6443 (1998).
39. Henry, S. *Study of the Nucleation and Growth of Feathery Grains in Aluminum alloys*, Ph.D. Thesis, EPFL Lausanne (1999).
40. Semoroz, A. *Experimental Study and Modeling of Nucleation and Growth During Solidification of Al and Zn Coatings*. Ph.D. Thesis, EPFL Lausanne (1999).
41. Semoroz, A., Durandet, Y. & Rappaz, M. EBSD characterization of dendrite growth directions, texture and misorientations in hot-dipped Al-Zn-Si coatings. *Acta Metall. Mater.* **49,** 529–541 (2001).
42. Von der Lage, F. & Bethe, H. A. A method for obtaining electronic eigenfunctions and eigenvalues in solids with an application to sodium. *Phys. Rev.* **71,** 612–622 (1947).
43. Fehlner, W. R. & Vosko, S. H. A product representation for cubic harmonics and special directions for the determination of the Fermi surface and related properties. *Can. J. Phys.* **54,** 2159–2169 (1976).
44. Gudgel, K. A. & Jackson, K. A. Oscillatory growth of directionally solidified ammonium chloride dendrites. *J. Cryst. Growth* **225,** 264–267 (2001).
45. Brener, E. & Levine, H. Growth of non-reflection-symmetric dendrites. *Phys. Rev. A* **43,** 883–887 (1991).

Acknowledgements

This research was supported by the US Department of Energy, Office of Basic Energy Sciences under contract DE-FG02-92ER45471 as well as the DOE Computational Materials Science Network program (T.H. and A.K.). The financial support of the Fonds National Suisse de la recherche scientifique, Bern, Switzerland (Grant No 200021-105144) is also gratefully acknowledged (F.G. and M.R.). Correspondence and requests for materials should be addressed to A.K.

Competing financial interests

The authors declare that they have no competing financial interests.